Ultrahigh-Amplitude Isolated Attosecond Pulses Generated in the Transmission Regime from Ultrathin Foil

Ruyu Pang,[1] Yunliang Wang,[1,*] Xueqing Yan,[2,3,4,†] and Bengt Eliasson[5,‡]

[1] *Department of Physics, School of Mathematics and Physics, University of Science and Technology Beijing, Beijing 100083, China*

[2] *State Key Laboratory of Nuclear Physics and Technology, and Key Laboratory of High Energy Density Physics (HEDP) of the Ministry of Education, Center for Applied Physics and Technology (CAPT), Peking University, Beijing 100871, China*

[3] *Beijing Laser Acceleration Innovation Center, Beijing 100871, China*

[4] *Collaborative Innovation Center of Extreme Optics, Shanxi University, Shanxi 030006, China*

[5] *Scottish Universities Physics Alliance (SUPA), Physics Department, John Anderson Building, University of Strathclyde, Glasgow G4 0NG, United Kingdom*

(Received 11 March 2022; revised 2 June 2022; accepted 21 June 2022; published 9 August 2022)

A coherent-synchrotron-emission regime of forward high-order harmonics generation (HHG) is proposed for the emission of an isolated unipolar half-cycle attosecond pulse by a three-color laser pulse impinging on ultrathin foil. A theoretical model is proposed for the electron nanobunching mechanism and the forward radiation, which is consistent with the numerical-simulation results. As the forward HHG does not need to penetrate from the front to the rear side of the target, the spectrum of the forward HHG has no low-frequency cutoff. The robustness of this regime is verified with different laser and foil plasma conditions as well as the two-dimensional effects. The robustness is also checked with similarity theory, which confirms that isolated attosecond pulses can be efficiently generated when the plasma density and the laser amplitude change simultaneously such that their ratio remains unchanged.

DOI: 10.1103/PhysRevApplied.18.024024

I. INTRODUCTION

The interaction of high-intensity laser pulses with very thin foil targets has attracted much attention for ion acceleration [1], high-order harmonics generation (HHG) [2], and attosecond-pulse generation [3]. The latter can provide unprecedented temporal and spatial resolution for the detection of ultrafast atomic and electronic phenomena [4,5]. Intense attosecond pulses can be generated by the locked-frequency HHG from laser interaction with solid targets [6]. The thin-foil model has been well developed for HHG from laser-driven thin foils [7,8], which is a solvable problem in the electrodynamics of HHG from laser-driven thin foil in the relativistic-oscillating-mirror (ROM) regime [9,10] and the relativistic-flying-mirror (RFM) regime [11].

The coupling mechanisms in the interaction of intense laser pulses with solid targets are related to the plasma-interface steepness and transit from the Brunel mechanism to chaotic dynamics [12]. Compared with laser-pulse-driven thick targets, the laser pulse impinging on the thin foil produces forward HHG emission that can be observed at the rear side of the thin foil. Forward HHG generated at the front side of the foil has a low-frequency cutoff in the spectrum because only harmonics above the maximum plasma frequency can propagate through the thin foil, which can be used to diagnose the generating plasma [13–16]. The forward harmonics can also be generated at the rear side by coherent wake emission (CWE) [17,18].

Forward attosecond pulses are also generated by coherent synchrotron emission (CSE) [19]. When the laser pulses interact with the thin foil, extremely dense electron nanobunches with a deltalike peak density distribution can be periodically formed at the front surface of the target and accelerated into the transmitted direction by the ponderomotive force of the laser [20], where the spectrum has a low-frequency cutoff as the generated harmonics are filtered by the high-density plasma foil and an attosecond-pulse train is emitted in the rear side of the foil. In general, the forward attosecond pulse has the structure of two distinct subpulses, which are emitted by both the primary electron sheet and the secondary electron sheet [3]. However, an isolated attosecond pulse is preferred for many

*ylwang@ustb.edu.cn
†x.yan@pku.edu.cn
‡bengt.eliasson@strath.ac.uk

applications of pump-probe techniques. More recently, the direct generation of isolated attosecond pulses in the transmission direction has been suggested, by using a few-cycle laser pulse interacting with a thin-foil target, where a portion of the backward electron sheet returns to the transmission to form the secondary electron sheet propagating in the forward direction [21,22]. However, the intensity of the forward attosecond pulse is usually much smaller than that of the incident pulse [3,21,22].

An advantage of the CSE mechanism is that the CSE spectrum typically has a slower decay scaling, $I(\omega) \propto \omega^{-4/3}$ or $I(\omega) \propto \omega^{-6/5}$ [23], which supports narrower pulses in time compared to the ROM and CWE regimes. Moreover, there is no limitation on the amplitude of the incident pulse in the CSE regime, which can withstand arbitrarily high fields. For the HHG in the relativistic regime, the higher laser intensities induce stronger nonlinearities, giving rise to higher harmonic efficiency. In the CSE regime, the formation and dynamics of an extremely dense electron sheet are crucial for the emission of attosecond pulses [19].

The aim of this paper is to propose a CSE regime in the transmission direction, where the intensity of the generated attosecond pulse can be made comparable to that of the incident pulse. The whole thin-foil target contributes to the formation of the electron nanobunch, the extremely dense electron sheet of which comes mainly from the rear surface of the foil. The spectrum of the generated forward harmonic has no low-frequency cutoff, as the generated forward harmonic does not need to penetrate from the front to the back of the target. The generated isolated attosecond pulse is a half-cycle unipolar pulse, which may be useful for pump-probe investigation of electron dynamics in solids and atoms by asymmetrical manipulation [21,22,24–26].

II. EMISSION MECHANISM OF FORWARD ATTOSECOND PULSE

A. Attosecond-pulse generation from electron sheet

We consider a new electron nanobunching regime, in which the thin-foil target is compressed by a three-color laser pulse to form an electron nanobunch. The formation and dynamics of the electron sheet are controlled by adjusting the relative phases between the three-color laser pulses. This nanobunching regime ensures that only one electron sheet contributes to the transmitted radiation, so that an ultraintense isolated attosecond pulse is generated in the transmission direction without the need for extra filters and gating techniques. As seen in Fig. 1(c), an ultrahigh-amplitude isolated attosecond pulse is emitted and propagates in the transmission direction, with a squared amplitude of $a_z^2 \approx 24\,000$ and a corresponding intensity of 4.8×10^{22} W/cm^2. The attosecond pulse is a half-cycle pulse and has a full width at half maximum

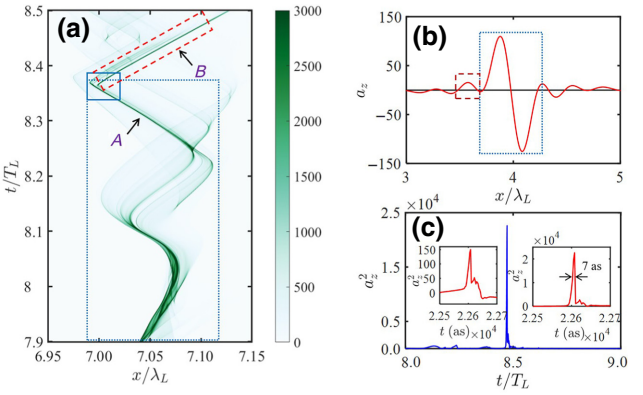

FIG. 1. (a) The spatiotemporal evolution of the normalized electron number density n_e/n_c from time $t = 7.9\ T_L$ to $t = 8.5\ T_L$. Extremely dense electron sheets are produced in the laser-plasma interaction, which result in forward attosecond-pulse generation. (b) The wave form of the normalized electric field $a_z = eE_z/(\omega_L m_e c)$ from the three-color laser pulses before it interacts with the foil. (c) The generated attosecond pulse in the transmission direction. The left inset shows a unipolar profile and the right inset shows a close-up of the attosecond pulse having a FWHM of about 7 as.

(FWHM) in time of about 7 as, as shown by the close-up of the inset in Fig. 1(c).

The fundamental mechanism for the isolated attosecond-pulse generation is studied using the particle-in-cell (PIC) code EPOCH [27]. A linearly polarized (along z) three-color laser pulse is launched in the x direction, normally incident on the ultrathin foil. The wavelength of the fundamental-frequency laser pulse is $\lambda_L = 800$ nm, with the angular frequency being $\omega_1 = \omega_L = 2\pi c/\lambda_L$ and the period being $T_L = \lambda_L/c = 2.67$ fs. The second- and the third-harmonic components have angular frequencies $\omega_2 = 2\ \omega_L$ and $\omega_3 = 3\ \omega_L$, respectively. The combined laser pulse has a normalized electric field $a_z = eE_L/(\omega_L m_e c)$ of the form $a_z = a_1 + a_2 + a_3$, where E_L is the electric field amplitude of the laser pulse, m_e is the electron rest mass, e is the unit charge, and c is the speed of light in vacuum. The three laser pulses have a Gaussian temporal envelope given by $a_{1,2,3} = a_{01,02,03} e^{-(t-T_L)^2/\tau^2} \sin[\omega_{1,2,3}(t - T_L) + \phi_{1,2,3}]$, where $\phi_1 = 6.055$ rad, $\phi_2 = 5.960$ rad, and $\phi_3 = 5.965$ rad are the phases of the fundamental and second- and third-harmonic frequency laser pulses, respectively. Here, $\tau = 0.5\ T_L$ and the duration $\sqrt{2\ln(2)}\tau = 0.59\ T_L$ is the FWHM in time of the three-color laser pulse. The normalized amplitudes of the fundamental and second and third harmonic pulses are $a_{01} = 50$, $a_{02} = 50$, and $a_{03} = 48$, respectively. The fundamental and second-harmonic frequency laser pulses have the same intensity $I_1 = I_2 = 5.35 \times 10^{21}$ W/cm^2. The intensity of the third-harmonic laser pulse is $I_3 = 4.9 \times 10^{21}$ W/cm^2. The length of the one-dimensional simulation box is 8 λ_L, which is resolved by 20 000 cells per wavelength and 100 quasiparticles per cell. The ultrathin

plasma foil is located in the region $7\ \lambda_L < x < 7.075\ \lambda_L$ with a high number density $n_e = 444\, n_c$, where the critical number density is $n_c = \omega_L^2 \epsilon_0 m_e / e^2$, where ϵ_0 is the electric permittivity in vacuum. The electrons and ions are uniformly distributed at first.

The wave form of the three-color laser pulse is the main factor in the formation and dynamics of an extremely dense electron sheet that are crucial for the emission of the isolated attosecond pulse. For the transmitted radiation, it is necessary to use at least a one-cycle driving laser pulse to ensure twice-per-cycle oscillation of the electron sheet. Only in this way can the electron sheet move in the direction of transmission. The wave form of the three-color laser pulses with the present carrier envelope phase (CEP) has only one large-amplitude cycle that rises and falls faster than for the fundamental-frequency laser pulse alone, which is similar to the case of two-color laser pulses [28]. It is the strongest cycle that primarily contributes to the formation of the electron sheet moving in the transmitted direction. The weak cycles on the rising side of the laser pulse only produce slight perturbations on the plasma front surface.

When the strongest cycle of the three-color laser pulses [as marked by a blue dotted rectangle in Fig. 1(b)] interacts with the foil plasma, the majority of the electrons from the thin foil are pushed from their equilibrium position toward the target by the Lorentz force. The Coulomb restoring force due to the displacement of the electrons increases and pulls them back when the Lorentz force decreases, which results in the relativistic electrons oscillating twice around the ion background, as marked by the blue dotted rectangle in Fig. 1(a). After the relativistic oscillation twice, these electrons pile up and form the self-organized dense electron nanobunch A shown in Fig. 1(a). When electron nanobunch A returns to the bulk plasma, those relatively dispersed electrons on the right-hand side of A converge into electron sheet B under the action of the Lorentz force from the driven laser pulses, as marked by the red dashed rectangular box in Fig. 1(b).

The emission process of the attosecond pulse is analyzed by the phase-space evolution in Fig. 2, which shows that the formation of the ultradense electron sheet B occurs at $t = 8.368\ T_L$ as the electron nanobunch returns to the target plasma. The position of the electron sheet B is illustrated by the green dotted line. After that, the electron sheet B is accelerated to an ultrarelativistic velocity by the electrostatic force and ponderomotive force, the strong charge-separation field a_x and the laser-pulse field a_z during this period being shown in Figs. 2(g)–2(i). During the acceleration of the electron sheet B, the longitudinal momentum of the sheet B grows constantly with time, during which the distribution takes the shape of a whip from $t = 8.368\ T_L$ to $t = 8.446\ T_L$, as shown in Figs. 2(a)–2(c). The transverse momentum decreases with time, as shown in Figs. 2(e) and 2(f) at $t = 8.407\ T_L$ and $t = 8.446\ T_L$, respectively. The

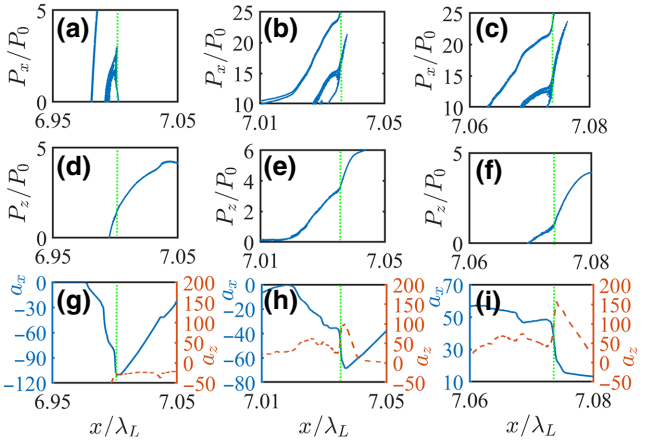

FIG. 2. The first row shows the electron longitudinal momentum distribution in phase space in the x-p_x plane at different times (a) $t = 8.368\ T_L$, (b) $t = 8.407\ T_L$, and (c) $t = 8.446\ T_L$. The nanobunching starts at $t = 8.368\ T_L$ and the longitudinal velocity of electron sheet B reaches its maximum at $t = 8.446\ T_L$. The second row (d)–(f) shows the electron transverse momentum distribution in phase space in the x-p_z plane at the different times. The third row (g)–(i) shows the charge-separation field a_x (blue solid line) and the laser-pulse field a_z (red dashed line) acting on electron sheet B at the different times. The green dotted line denotes the position of electron sheet B at different times.

lateral acceleration in the z direction reaches a maximum value as the longitudinal velocity reaches a velocity close to c at $t = 8.446\ T_L$. The transverse acceleration is due to the weak half cycle of the laser pulses marked by the red dashed box in Fig. 1(a), which is also confirmed in Fig. 2(i), where the strong transverse field is about $a_z \sim 75$ at time $t = 8.446\ T_L$.

B. Theoretical analysis

The high-frequency spectrum of the forward pulse is determined by the transverse nonlinear electric current of the ultrathin foil as [7]

$$J_z(x,t) = -2\sigma_0 \delta\left(x - x_0(t)\right) v_z(t). \tag{1}$$

Here, we consider a deltalike peak electric current density distribution and $x_0(t)$ is the position of the electron sheet B at time t. The transverse velocity is $v_z(t) = A_z(t)/\gamma$, where the relativistic factor is $\gamma = \sqrt{1 + A_z^2}$, in which A_z is the vector potential of the driven laser pulse and is normalized by $m_e c^2/e$. The dimensionless areal charge density is $\sigma_0 = \pi n_e d_0/\lambda$, where d_0 is the thickness of the foil and λ is the wavelength of the driven laser pulse [7]. The relationship between the dimensionless electric field a_z and the dimensionless vector potential A_z is $a_z = -dA_z/dt$. For convenience, we use the dimensionless vector potential A_z to investigate the high-frequency spectrum of the forward pulse. The dimensionless vector potential of the

three-color laser pulse $A_z = A_1 + A_2 + A_3$ is given as

$$A_z(t) = A_{01}e^{-\frac{t^2}{\tau^2}}\cos(2\pi t + \phi_1) + A_{02}e^{-\frac{t^2}{\tau^2}}\cos(4\pi t + \phi_2) + A_{03}e^{-\frac{t^2}{\tau^2}}\cos(6\pi t + \phi_3), \quad (2)$$

where τ is related to the FWHM $\sqrt{2\ln(2)}\tau$ in time of the three-color laser pulses. t and τ are all normalized by λ/c. The space argument x is normalized by λ. A_{01}, A_{02}, and A_{03} are the normalized vector potential amplitudes of the fundamental and second- and third-harmonic pulses, respectively. The first-order approximation $\gamma \approx \gamma_0$ gives the transverse velocity as

$$v_z = v_{z0} - \alpha t^2, \quad (3)$$

where the coefficients $v_{z0} = \gamma_0^{-1}[A_{01}(1-\phi_1^2/2) + A_{02}(1-\phi_2^2/2) + A_{03}(1-\phi_3^2/2)]$ and $\alpha = \gamma_0^{-1}[A_{01}(4\pi^2\tau^2 + 2 - \phi_1^2)/2\tau^2 + A_{02}(16\pi^2\tau^2 + 2 - \phi_2^2)/2\tau^2 + A_{03}(36\pi^2\tau^2 + 2 - \phi_3^2)/2\tau^2]$. Here, the first power term of time t is omitted as we focus on the high-frequency spectrum of the forward pulse. As the electron sheet B has ultrarelativistic velocity, the absolute velocity normalized by c is close to 1. Then, by using the relationship $v_x^2 + v_z^2 = v^2$, where v_x is the longitudinal velocity of the electron sheet B, we can obtain the position $x_0(t) = \int v_x dt$ of the electron sheet B as

$$x_0(t) = \sqrt{v^2 - v_{z0}^2}\,t + \frac{\alpha v_{z0}}{\sqrt{v^2 - v_{z0}^2}}\frac{t^3}{3} - \frac{\alpha^2}{2\sqrt{v^2 - v_{z0}^2}}\frac{t^5}{5}. \quad (4)$$

Here, the normalized velocity is close to 1 ($v \sim 1$). The transmitted radiation can be determined by the transverse-current distribution $J_z(x,t)$ that is normalized by $en_c c$, where the transverse-current density distribution is assumed to be unchanged. The transmitted field is given as

$$E(t) = -\pi\int J_z(x, t+x)dx = 2\sigma_0\pi\int v_z(t+x)\delta\left(x - x_0(t+x)\right)dx. \quad (5)$$

The Fourier transform of the field $E(t)$ gives the spectrum of the transmitted radiation as [29]

$$I(\omega) = 8\sigma_0\alpha^2\pi^4\left(\beta\omega\right)^{-\frac{6}{5}}\left|\mathrm{Ai}_2''(\xi)\right|^2, \quad (6)$$

where $\xi = \omega^{4/5}(1 - \sqrt{v^2 - v_{z0}^2})(2\sqrt{v^2 - v_{z0}^2}/\alpha^2)^{1/5}$, $\beta = \alpha^2/2\sqrt{v^2 - v_{z0}^2}$, and $\mathrm{Ai}_2''(\xi) = (1/2\pi)\int \tau^2 e^{i\xi\tau}e^{i\tau^5/5}d\tau$ is the second derivative of the generalized Airy function [29] of the second kind. Here, we use the fact that $\left|\widetilde{\delta}(\omega)\right|^2 \sim 1$, where $\widetilde{\delta}(\omega)$ is the Fourier transform of the δ function. The spectrum of HHG in the transmission direction in the simulation shows that the attosecond pulse has up to 10 000 higher-order harmonic components, as shown in Fig. 3(a), which is consistent with the above theoretical prediction and confirms the $I(\omega) \propto \omega^{-6/5}$ scaling law for high frequencies in the spectrum. In general, the spectrum of HHG of the reflected radiation has been shown to have a $I(\omega) \propto \omega^{-6/5}$ scaling law [29], while the spectrum of HHG of the transmitted radiation from a thin foil has a $I(\omega) \propto \omega^{-4/3}$ scaling law [20]. For our attosecond pulse from the ultrathin target, the dense electron sheet B comes mainly from the rear surface of the thin foil, as shown in Fig. 3(b). Accordingly, the forward HHG does not need to penetrate from the front to the rear side of the target. In our geometry, the high-density plasma is no longer a high-pass frequency filter. Then, the spectrum of the forward HHG does not have a low-frequency cutoff, as can be seen in Fig. 3(a).

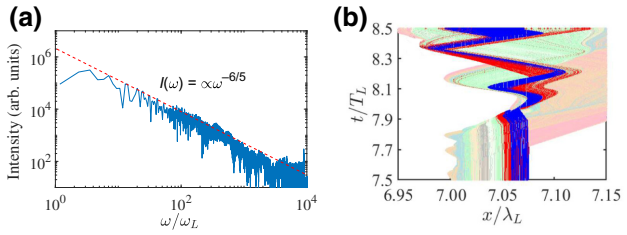

FIG. 3. (a) The harmonic spectra of the transmitted isolated attosecond-pulse radiation behind the target. The attenuation of the spectrum follows $I(\omega) \propto \omega^{-6/5}$. (b) The electron trajectory in the x-t plane.

III. MECHANISM OF ELECTRON NANOBUNCHING

A. Numerical analysis of nanobunching

From the insight into the structure of the dense electron nanobunch A as illustrated in Fig. 4(a), the relatively dispersed electrons on the right-hand side converge into dense electron sheet B just as the bunch reverses its direction toward the target. In the CSE regime, the formation and dynamics of the very dense electron sheet B are crucial for the emission of a forward attosecond pulse.

The physical mechanisms of electron sheets A and B are illustrated in Figs. 4(b) and 4(c). When the electron nanobunch A is moving in the reflection direction with a negative longitudinal momentum, the resultant Coulomb and Lorentz forces $f_E + f_B$ [represented by red dots in Fig. 4(b)] acting on those electrons on the right-hand side of electron nanobunch A decrease gradually from left to right, which can be seen from three representative spatial

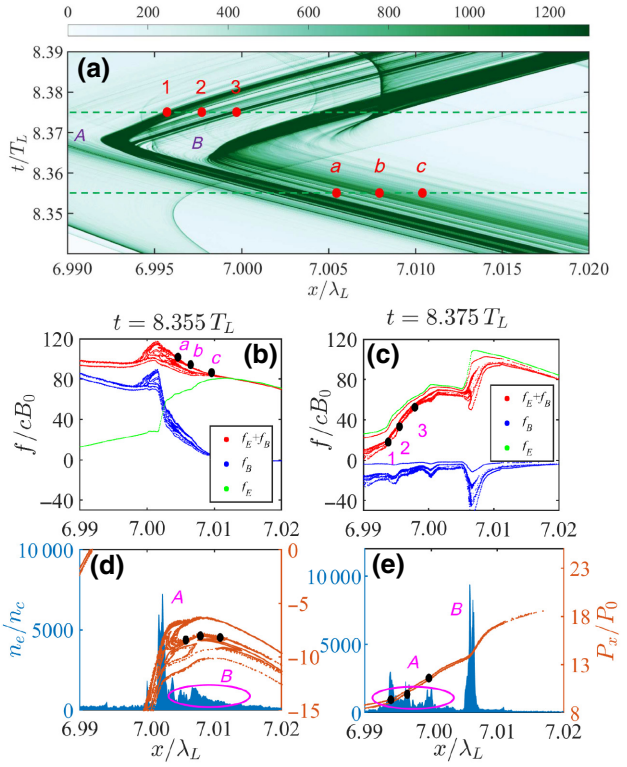

FIG. 4. (a) A close-up of the spatiotemporal evolution of the normalized electron number density n_e/n_c of the blue box in the Fig. 1(a), where we mark six representative spatial positions: $x = 6.995\,\lambda_L$, $x = 6.997\,\lambda_L$, and $x = 6.999\,\lambda_L$, marked as 1, 2, and 3 at time $t = 8.375\,T_L$; and $x = 7.005\,\lambda_L$, $x = 7.008\,\lambda_L$, and $x = 7.011\,\lambda_L$, marked as a, b, and c at time $t = 8.355\,T_L$ with solid red dots. (b),(d) The Coulomb force f_E (green dotted line), the Lorentz force f_B (blue dotted line), and the resultant force $f_E + f_B$ (red dotted line) acting on electron nanobunch B at time $t = 8.355\,T_L$ and on electron nanobunch A at time $t = 8.375\,T_L$, respectively. (c),(e) The electron number density and the longitudinal momentum distribution of the nanobunches at time $t = 8.355\,T_L$ and $t = 8.375\,T_L$, respectively. The force is normalized by cB_0 with $B_0 = m_e\omega/c$. The momentum $P_x = \gamma m_e v_x$ is normalized by $P_0 = m_e c$, where v_x is the longitudinal velocity of the electrons.

positions marked as a, b, and c in Fig. 4(b), the electron longitudinal momenta of which differ only slightly, as shown in Fig. 4(c). As the Coulomb force f_E [represented by green dots in Fig. 4(b)] acting on those electrons on the right-hand side of electron nanobunch A increases gradually from left to right, the Lorentz force f_B [represented by blue dots in Fig. 4(b)] from the laser pulse, which decreases gradually from left to right as the incident laser field is gradually shielded by the dense nanobunches from left to right, plays a leading role in the formation of electron sheet B. Since the resultant force $f_B + f_E$ on the electrons is in the right-hand direction, contrary to the direction of motion, the relatively dispersed electrons that are on the right of electron sheet A will converge into electron sheet B.

By contrast, at time $t = 8.375\,T_L$, the resultant force $f_E + f_B$ acting on the electrons of nanobunch A increases gradually from left to right, while the magnitude of the negative longitudinal momentum increases gradually from left to right. Accordingly, the electron on the right deflects much earlier than the electron on the left of A. At the end of the strong relativistic oscillation twice, the electron nanobunch A is dispersed during acceleration by the electrostatic restoring force after it returns to the target, as can clearly be seen in Figs. 4(d) and 4(e). We select the moment $t = 8.375\,T_L$ to show the process of spreading of A, where it can be seen that the positive longitudinal momentum of the electrons at the three representative spatial positions (marked as 1, 2, and 3) gradually increases from left to right as shown in Fig. 4(d). Moreover, the electrostatic field force f_E [represented by green dots in Fig. 4(d)] acting on the electrons also increases from left to right. There is little difference in the magnitude of the Lorentz force f_B acting on the electrons at different positions. Therefore, it can be concluded that the electrons on the right will run faster than those on the left, which results in the spreading of A during acceleration. The electron density to the left of electron sheet B is greatly reduced, as shown in Fig. 4(e), which reduces the shielding effect on the laser field. As a result, the weak half cycle of the laser pulse marked by the red dashed box in Fig. 1(a) can easily penetrate nanobunch A and provide a large transverse perturbation on electron sheet B.

B. Theoretical model of nanobunching

Here, we analytically investigate the formation of electron sheet B in the laser-plasma interactions in the ultrarelativistic limit. From the numerical-simulation results, one can see that the relativistic oscillation is crucial for the formation of electron sheet B. The dynamics of the electron sheet B are governed by the momentum equation

$$\frac{d(\gamma v_x)}{dt} = -2\pi\left(a_x - v_z B_y\right), \tag{7}$$

where the electric field a_x, the magnetic field B_y, and the velocity (v_x, v_z) are normalized by $m_e\omega_L c/e$, $m_e\omega_L/e$, and c, respectively. The time argument t is normalized by λ/c. We assume that the transverse laser field and the transverse momentum of the electrons remain basically unchanged in the process of electron convergence. Then Eq. (7) can approximately denote the formation process of the electronic sheet. The electrostatic electric field can be written as

$$a_x(x(t), t) = 2\pi \int_{-\infty}^{x(t)} (Z_i n_{i0} - n_e(x', t))dx', \tag{8}$$

where Z_i is the charge number of the ion. The unperturbed ion number density n_{i0} and the electron number density

n_e are normalized by n_c. The space argument x and x' are normalized by λ. Here, we assume that the ions remain stationary under the action of the driven laser pulse. The total derivative of the electrostatic electric field with respect to time is

$$\frac{da_x(x(t),t)}{dt} = 2\pi\left[\frac{dx}{dt}(Z_i n_{i0} - n_e(x,t)) + \int_{-\infty}^{x(t)} \frac{\partial(Z_i n_{i0} - n_e(x',t))}{\partial t} dx'\right]. \quad (9)$$

Since the ion number density is constant, Eq. (9) simplifies as follows:

$$\frac{da_x(x(t),t)}{dt} = 2\pi\left[v_x\,(Z_i n_{i0} - n_e(x,t)) - \int_{-\infty}^{x(t)} \frac{\partial n_e(x',t)}{\partial t} dx'\right]. \quad (10)$$

In a fluid picture, the electrons satisfy the continuity equation of the fluid, $v_x n_e(x,t) + \int_{-\infty}^{x}[\partial n_e(x',t)/\partial t]dx' = 0$. Then, Eq. (10) can be simplified as $da_x/dt = 2\pi\, v_x Z_i n_{i0} = 2\pi\, v_x n_{e0}$, where n_{e0} is the unperturbed equilibrium electron number density satisfying the charge neutrality $n_{e0} = Z_i n_{i0}$. Then, from Eq. (7) and the above results, one can obtain the equation governing the longitudinal dynamics as

$$\frac{d^2 p_x}{dt^2} = \frac{-4\pi^2 n_{e0} p_x}{\sqrt{1+p_x^2+p_z^2}}, \quad (11)$$

where we assume that the transverse laser magnetic field and the transverse momentum of the electrons remain unchanged during the nanobunching when the bunch reverses its direction toward the target. If the longitudinal momentum of the electron sheet B is obtained from Eq. (11), the spatial coordinates of the electron sheet B at any time can be obtained as

$$x(t) = \int_0^t \frac{p_x(t')}{\sqrt{1+p_x(t')^2+p_z^2}} dt'. \quad (12)$$

We take the time derivative of Eq. (12) and use Eq. (11) in Eq. (12) as follows:

$$\frac{dx(t)}{dt} = \frac{p_x(t)}{\sqrt{1+p_x(t)^2+p_z^2}} = -\frac{1}{4\pi^2 n_{e0}}\frac{d^2 p_x}{dt^2}. \quad (13)$$

Integrating Eq. (13) once, we obtain that $x(t) = C_1 - (1/4\pi^2 n_{e0})dp_x(t)/dt$, where C_1 is the integration constant. Assuming a coordinate system such that $dp_x/dt = 0$ at $t = 0$, we have $C_1 = 0$ and

$$\frac{dp_x(t)}{dt} = -4\pi n_{e0} x(t). \quad (14)$$

We multiply Eq. (11) by dp_x/dt as follows:

$$\frac{1}{2}\frac{d}{dt}\left(\frac{dp_x(t)}{dt}\right)^2 = -4\pi n_{e0}\frac{d}{dt}\sqrt{1+p_x(t)^2+p_z^2}. \quad (15)$$

Integrating Eq. (15) once, we obtain that $1/2\,(dp_x(t)/dt)^2 = C_2 - 4\pi n_{e0}\sqrt{1+p_x(t)^2+p_z^2}$, where C_2 is the integration constant. We assume $p_x(t) = p_{x0}$ at $t = 0$, where $dp_x/dt = 0$. Then the constant is $C_2 = 4\pi n_{e0}\sqrt{1+p_{x0}^2+p_z^2}$. We have

$$\frac{1}{2}\left(\frac{dp_x(t)}{dt}\right)^2 = 4\pi n_{e0}\left(\sqrt{1+p_{x0}^2+p_z^2} - \sqrt{1+p_x(t)^2+p_z^2}\right). \quad (16)$$

Using Eq. (14) in Eq. (16), after simplification we obtain the phase-space relation as

$$2\pi n_{e0} x^2(t) + \sqrt{1+p_x(t)^2+p_z^2} = \sqrt{1+p_{x0}^2+p_z^2}, \quad (17)$$

which gives $x(t)$ as a function of $p_x(t)$ for different values p_{x0} and p_z. Both the phase-space and time-space evolution of the electron trajectory are dependent on the initial conditions, which can be obtained from the simulation results shown in Figs. 4(b) and 4(c). The solution of the second-order differential in Eq. (11) gives the nanobunching process in Fig. 5(a), where we use the initial conditions $p_z = -2.5$, $p_x = -7.5$, -7.6, -7.7, and -7.8, and $dp_x/dt = 110$, 109, 108, and 107. Figure 5(b) is used to explain the divergence mechanism of electron nanobunch A as shown in Fig. 4(a), where the initial conditions are taken as $p_z = -4$, $p_x = -10$, -9.5, -9, and -8.5, and $dp_x/dt = 100$, 102, 104, and 106, which can be obtained from Figs. 4(d) and 4(e). The main reason for the divergence of the electron sheet is that the Lorentz forces of the laser field on the electrons at different spatial positions and the longitudinal velocity of those electrons in A are quite different. We can see that the theoretical model agrees well with the simulation results with regard to the nanobunching process of B and the divergence mechanism of A.

IV. SIMILARITY LAW OF FORWARD ATTOSECOND PULSE

We verify the robustness of our CSE regime of the forward attosecond pulse with the help of similarity parameters $S = n_e/a_m$, where the electron density n_e is normalized by critical density n_c and a_m is the normalized maximum

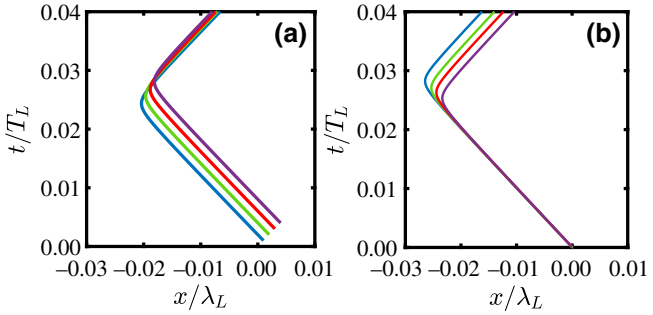

FIG. 5. The electron trajectory in the x-t plane from the analytical model. (a) The nanobunching model for explaining the convergence mechanism of the electrons. (b) The model for explaining the divergence mechanism of the electron nanobunch.

amplitude of the strongest cycle of the three-color laser pulses. Similarity theories are useful to describe electron dynamics in laser-plasma interaction processes [30] and have been used to investigate the HHG of the reflected radiation in the ROM regime [31,32]. Here, we show that the forward HHG by the laser-driven ultrathin target also has a similarity law in the CSE regime.

We numerically verify the similarity theory about the forward attosecond-pulse emission in the CSE regime. The three-color laser-amplitude and plasma-electron-density parameters are shown in Table I. From Fig. 6(a), we can see that the isolated unipolar attosecond-pulse emission has similarity states and results with approximately equal similarity parameters $S \sim 3.51$, although a_m and n_e are different in these six cases. When the plasma density and the laser amplitude change simultaneously to ensure that the similarity parameter is constant, the electron nanobunching dynamics and the forward attosecond-pulse emission process remain similar. The three-color laser amplitude and the electron density are given in Table I, where we can see that the value of the similar parameters is about $S \sim 3.51$. The phases of the three-color laser pulses are taken as $\phi_1 = 6.055$ rad, $\phi_2 = 5.960$ rad, and $\phi_3 = 5.965$ rad. The thickness of the target is 60 nm for all cases. For all six cases, the generated forward attosecond pulses are all isolated and unipolar pulses. From the overall trend of Fig. 6(a), the greater the amplitude of the driving laser pulse, the greater is the amplitude of the generated attosecond pulse, of which the durations at FWHM are all below 10 as, as shown by the close-up of the attosecond pulse with regard to the six cases in Figs. 6(b)–6(g). For the case of $n_e = 800n_c$, the attosecond pulse has an intensity of up to $I \sim 8.2 \times 10^{22}$ W/cm^2 and a FWHM of about 3.5 as.

The longitudinal dynamics of the ultrathin foil are determined by the combined effects of the laser ponderomotive force and the electrostatic force. For a given foil thickness d_0, the value of the similar parameters can be estimated by the balance between the laser ponderomotive force and the

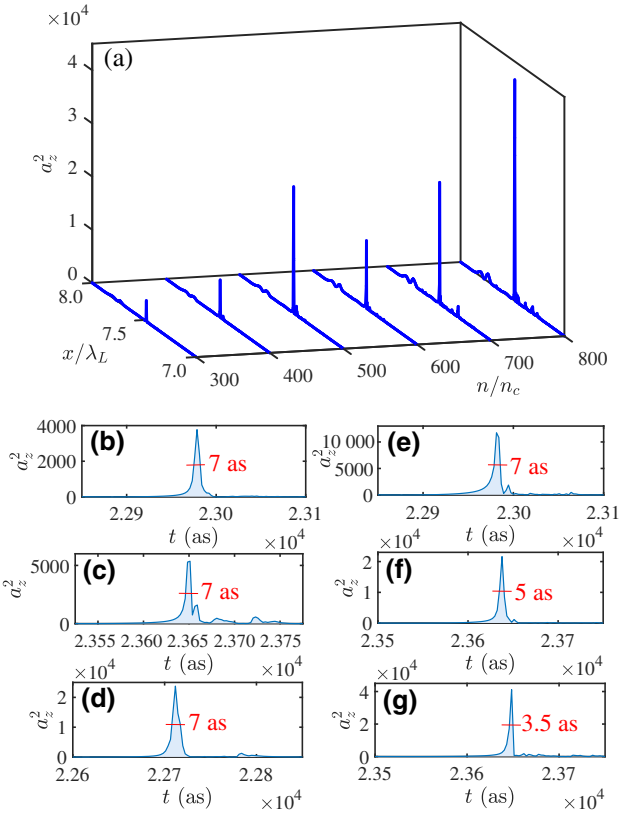

FIG. 6. (a) The similarity law of the forward attosecond-pulse generation in the CSE regime demonstrated numerically by six cases. The close-up of the attosecond pulse shows a FWHM of (b) 7 as for $n_e = 300n_c$, (c) 7 as for $n_e = 400n_c$, (d) 7 as for $n_e = 500n_c$, (e) 7 as for $n_e = 600n_c$, (f) 5 as for $n_e = 700n_c$, and (g) 3.5 as for $n_e = 800n_c$.

electrostatic force [7,32]

$$(1 + R)a_m = 2\pi \frac{d_0}{\lambda} n_e, \tag{18}$$

where R is the laser reflectivity [7] and d_0 is the thickness of the foil target. Here, we assume that the whole target is compressed such that it is so thin that the number density of the electrons can be regarded as a deltalike peak density

TABLE I. The similarity parameters $S = n_e/a_m$ of forward attosecond-pulse generation in the CSE regime. a_m is the maximum amplitude of the strongest cycle of the three-color laser pulses.

n_e	a_{01}	a_{02}	a_{03}	a_m	S
300	35	32	33	84.37	3.56
400	44.5	45	43.5	112.8	3.55
500	56.77	56.78	54.51	142.4	3.51
600	68.1	68.6	65.55	171.5	3.50
700	80.1	80	78	201.8	3.47
800	91	92	87	228.9	3.49

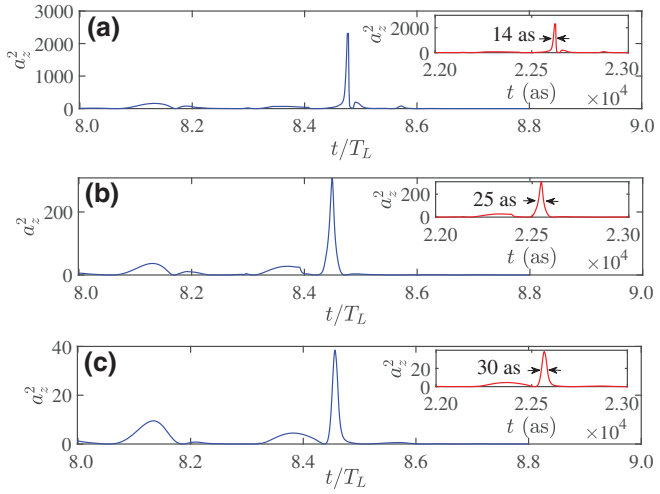

FIG. 7. The forward attosecond-pulse generation from the interaction of the three-color laser pulses with foils having different plasma densities: (a) similarity parameter $S = 3.63$, duration 14 as, for $n_e = 200n_c$, $a_1 = 22$, $a_2 = 22$, and $a_3 = 21$; (b) similarity parameter $S = 4.08$, duration 25 as, for $n_e = 100n_c$, $a_1 = 10$, $a_2 = 10$, and $a_3 = 9$; (c) similarity parameter $S = 4.78$, duration 30 as, for $n_e = 50n_c$, $a_1 = 4.4$, $a_2 = 4.4$, and $a_3 = 3.6$.

distribution. Accordingly, the maximum depletion length is approximately equal to the foil thickness d_0. Then, we can obtain the approximate value range of the similarity parameter S as

$$\frac{\lambda}{2\pi d_0} < S < \frac{\lambda}{\pi d_0}. \tag{19}$$

From Eq. (19), we can obtain the similarity parameter $2.1 < S < 4.2$ with the wavelength $\lambda = 800$ nm and the foil thickness $d_0 = 60$ nm.

In order to further verify the similarity law of forward attosecond-pulse generation scheme at lower laser intensity, we consider the interaction of the three-color laser pulses with the near-critical-density foil plasma. From Table I, we see that the similarity parameter S increases slightly with the decrease of the laser-pulse intensity, which is due to the fact that the relativistic effects on the plasma density also decrease as the intensity decreases. The self-induced relativistic transparency effect is reduced. As expected, the simulation at lower laser intensity shows that the isolated attosecond pulses can also be emitted with a larger similarity parameter S, as shown in Fig. 7. In this CSE regime, the HHG is coherently superimposed to produce high-quality isolated attosecond pulses. As the stronger nonlinearities give indeed rise to the higher harmonic efficiency, the higher harmonic efficiency will decrease with the decrease of the laser intensity, which will cause the pulse duration to become larger, as shown in Fig. 7.

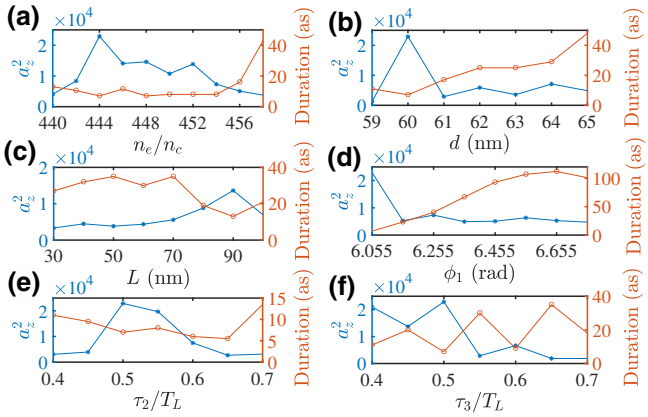

FIG. 8. The durations (in attoseconds) at FWHM and the normalized intensities a_z^2 of the attosecond pulses as functions of (a) the plasma densities n_e, (b) the thickness d of the foil, (c) the length of the linear density ramp of the preplasma, (d) the phase of the fundamental-frequency laser pulse, (e) the duration $\sqrt{2\ln(2)}\tau_2$ of the second-harmonic laser pulse, and (f) the duration $\sqrt{2\ln(2)}\tau_3$ of the third-harmonic laser pulse. Here, for simplicity, we take τ_2 or τ_3 as the horizontal ordinate.

V. ROBUSTNESS OF FORWARD ATTOSECOND-PULSE GENERATION SCHEME

We discuss the robustness of the forward attosecond-pulse generation scheme with different laser and foil plasma conditions as well as including multidimensional effects. First, we check the robustness by varying the density, thickness, and length of the linear density ramp at the front of the target. We keep the other parameters the same as in Fig. 1. We can see in Fig. 8(a) that the durations are all below 16 as and intensity $a_z^2 > 4058$ for a plasma density of $440\,n_c < n_{e1} < 456\,n_c$. The appropriate foil-thickness region can also be determined by the balance between the laser ponderomotive force and the electrostatic force. The durations are all below 29 as and intensity $a_z^2 > 2898$ for a thickness of the target in the range 60 nm $< d <$ 64 nm, as shown in Fig. 8(b). When the thickness of the target increases, the duration at FWHM of the attosecond pulse will increase from about 10 as to 30 as. When the target is too thin, attosecond pulses are no longer generated, which is due to the fact that the driven laser pulse can penetrate the target and the electron nanobunch is no longer formed. The additional preplasma at the front of the foil is also considered by varying the length of the linear density ramp as illustrated in Fig. 8(c), which shows that the durations are all below 35 as and intensity $a_z^2 > 3329$ for length L of the linear density ramp in the range 30 nm $< L <$ 100 nm.

We also perform a series of simulations to study the effects of different laser parameters on our scheme. In Fig. 8(d), the phase ϕ_1 of the fundamental-frequency laser pulse varies from $\phi_1 = 6.055$ rad to $\phi_1 = 6.655$ rad, while the other parameters are kept the same as in Fig. 1. With

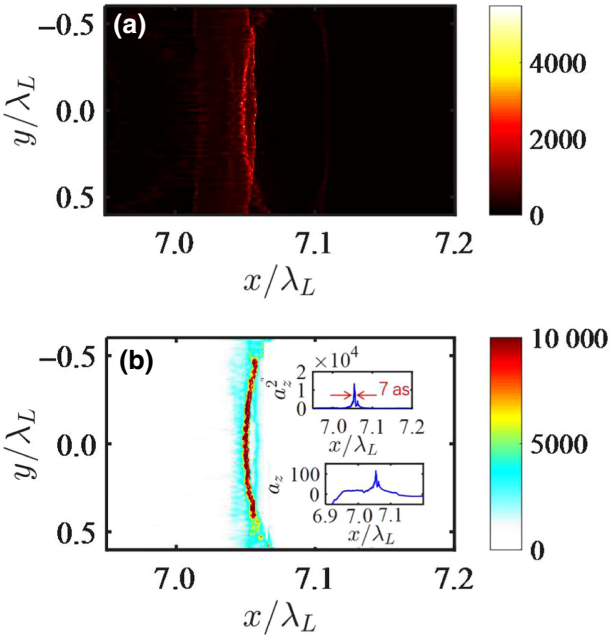

FIG. 9. A two-dimensional (2D) simulation on the transmitted attosecond-pulse generation. (a) The density of electron sheet n_e denoting the generation of the forward attosecond pulse. (b) The generated isolated attosecond pulse in the transmitted direction without the need for extra filters, where the two insets show that the FWHM of a_z^2 is about 8 as and the attosecond pulse has a half-cycle profile.

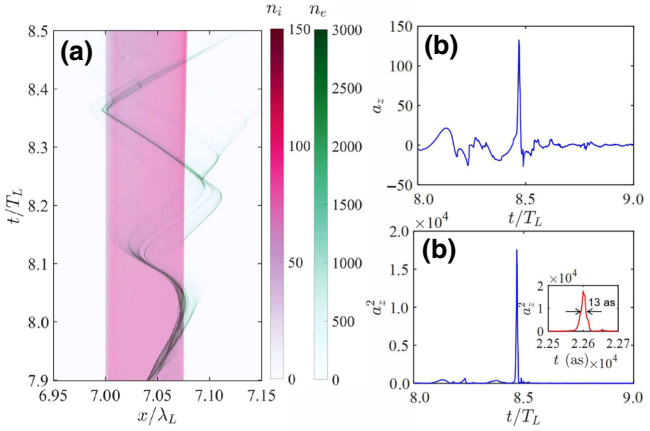

FIG. 10. (a) The spatiotemporal evolution of the electron number density n_e/n_c and the ion number density from time $t = 7.9\ T_L$ to $t = 8.5\ T_L$. (b) The half-cycle profile of the forward attosecond pulse a_z. (c) The profile of the intensity of the attosecond pulse a_z^2 and an inset with a close-up of the attosecond pulse having a FWHM of about 13 as.

the change of phase ϕ_1, the duration of the attosecond pulse increases from below 10 as to 112 as and intensity $a_z^2 > 4746$. We also consider the effects of the durations $\sqrt{2\ln(2)}\tau_2$ of the second-harmonic laser pulse and $\sqrt{2\ln(2)}\tau_3$ of the third-harmonic frequency laser pulse, as shown in Figs. 8(e) and 8(f), respectively. The durations of the attosecond pulse are all below 13.5 as and intensity $a_z^2 > 2686$ for τ_2 in the range $0.4T_L < \tau_2 < 0.7T_L$, as shown in Fig. 8(e). When τ_3 of the third-harmonic frequency laser pulse varies from $0.4T_L$ to $0.7T_L$ as shown in Fig. 8(f), the durations of the attosecond pulse are all below 35 as and intensity $a_z^2 > 1866$.

To consider multidimensional effects, we also perform a two-dimensional (2D) simulation on the transmitted attosecond-pulse generation, where the plasma foil is the same as in Fig. 1 but is located between $x = 7.0\ \lambda_L$ and $x = 7.075\ \lambda_L$ and between $y = -18\ \lambda_L$ and $y = 18\ \lambda_L$. The simulation box is $8\ \lambda_L \times 36\ \lambda_L$, containing $40\,000 \times 7\,200$ cells. The number of particles per cell is 100 in the foil target plasma. The laser pulses have transverse Gaussian profile e^{-y^2/w_0^2}, with $w_0 = 6.25\lambda_L$. The longitudinal profile of the laser pulses is the same as that in Fig. 1. The dynamics of the electron sheet and the emission process of the attosecond pulse are almost identical to the one-dimensional case, because the interaction is too short to cause any multidimensional instabilities. The forward attosecond pulse is generated by the electron sheet that is accelerated in the longitudinal direction and perturbed transversely. The amplitude of the forward attosecond pulse reaches the maximum at time $t = 8.446\ T_L$ and the duration is about 8 as, which is illustrated by snapshots at time $t = 8.446\ T_L$ in Fig. 9. We also show the forward attosecond pulse as insets in Fig. 9(b) at $y = 0$ and $t = 8.446\ T_L$ without the extra filters, which shows that the FWHM of a_z^2 is about 8 as and that the attosecond pulse has a half-cycle profile.

In the above simulations, the ions are assumed to be immobile, as the duration of the interaction between the laser and the target is very short. We also perform simulations with mobile ions in order to check the rationality of this assumption, as illustrated in Fig. 10. The parameters of the laser pulses and plasma are the same as those in Fig. 1. As can be seen from Fig. 10, the ions are only slightly pushed from their equilibrium position toward the transmitted direction by the ponderomotive force of the laser pulses, which shows that there is no oscillation for the ions. From the comparison between Figs. 1(a) and 10(a), the spatiotemporal evolution of the electron number density is almost identical to the case in which the ions are assumed to be immobile. The extremely dense electron sheet is also produced in the laser-plasma interaction and is responsible for the attosecond pulse in the CSE regime. Accordingly, the forward attosecond pulses are also generated in the case of mobile ions, which also have a half-cycle profile [shown in Fig. 10(b)] and the FWHM of a_z^2 is about 13 as [shown in Fig. 10(c)] and is slightly larger than the case (7 as) shown in Fig. 1.

VI. DISCUSSION AND CONCLUSIONS

In this paper, an ultrathin foil regime of forward isolated unipolar attosecond-pulse emission is proposed by using a three-color laser pulse impinging an ultrathin foil, the thickness of which is approximately equal to the maximum depletion length. As a result, the secondary electron sheet will not be formed. In general, the secondary electron sheet contributes to coherent synchrotron radiation besides the primary electron sheet [3]. As the primary and secondary electron sheets both contribute to the transmitted radiation, the attosecond pulses have two distinct subpulses. The distinct subpulse structure in the forward attosecond pulse no longer appears in our ultrathin foil regime.

The robustness of the attosecond-pulse generation scheme is checked with different laser and foil plasma conditions and with regard to the multidimensional effects. The density, the thickness, the length of the linear density ramp at the front of the target, the phase ϕ_1 of the fundamental-frequency laser pulse, and the durations of the second and third harmonics are varied. 2D simulation shows that the dynamics of the electron sheet and the emission process of the attosecond pulse are similar to those of the one-dimensional case. The robustness of the regime is also verified with the help of similarity theory, where the isolated unipolar attosecond pulses are emitted with approximately equal similarity parameters $S \sim 3.51$ for different laser amplitudes a_0 and electron densities n_e in all cases. For the case of $n_e = 800n_c$, the attosecond pulse has an intensity of up to $I \sim 8.2 \times 10^{22}$ W/cm^2 and a FWHM of about 3.5 as.

For reflected radiation in the CSE regime, the intensity of the emitted attosecond pulse can be comparable with or much larger than that of the incident pulse, while for transmitted radiation in the CSE regime, the intensity of the attosecond pulse is usually smaller than that of the incident pulse [3,21,22]. In this paper, the intensity of the forward attosecond pulse generated from the ultrathin foil regime is comparable to that of the incident pulse. Instead of electrons oscillating only at skin depth in the front side of the plasma, in the ultrathin foil regime all electrons in the plasma target oscillate twice under the action of the strongest cycle of the three-color laser pulses. After that, a dense electron sheet with maximum density $> 11000\, n_c$ is formed and accelerated to ultrarelativistic velocity, while being transversely perturbed by the weak half cycle of the laser pulse. As a result, an isolated unipolar attosecond pulse is emitted. Since the extremely dense electron sheet comes mainly from the rear surface of the thin foil, the forward HHG does not need to penetrate from the front of the target to the rear side of the target and the spectrum of the forward HHG has no low-frequency cutoff.

The data that support the results of this study are available on request from the authors.

ACKNOWLEDGMENTS

This research was supported by the National Natural Science Foundation of China (NSFC) (Grant No. 11974043) and the Fundamental Research Funds for the Central Universities (Grant No. FRF-BR-19-002B). X. Y. acknowledges support by the National Natural Science Foundation of China (Grant No. 11921006) and the National Grand Instrument Project (Grant No. 2019YFF01014400). The work of B.E. was carried out partially within the framework of the EUROfusion Consortium. We acknowledge useful discussions with Dr. Y. R. Shou and Professor J. Q. Yu.

[1] T. Esirkepov, M. Borghesi, S. V. Bulanov, G. Mourou, and T. Tajima, Highly Efficient Relativistic-Ion Generation in the Laser-Piston Regime, Phys. Rev. Lett. **92**, 175003 (2004).

[2] U. Teubner, K. Eidmann, U. Wagner, U. Andiel, F. Pisani, G. D. Tsakiris, K. Witte, J. Meyer-ter-Vehn, T. Schlegel, and E. Förster, Harmonic Emission from the Rear Side of Thin Overdense Foils Irradiated with Intense Ultrashort Laser Pulses, Phys. Rev. Lett. **92**, 185001 (2004).

[3] S. Cousens, B. Reville, B. Dromey, and M. Zepf, Temporal Structure of Attosecond Pulses from Laser-Driven Coherent Synchrotron Emission, Phys. Rev. Lett. **116**, 083901 (2016).

[4] T. Pfeifer, C. Spielmann, and G. Gerber, Femtosecond x-ray science, Rep. Prog. Phys. **69**, 443 (2006).

[5] F. Krausz and M. Ivanov, Attosecond physics, Rev. Mod. Phys. **81**, 163 (2009).

[6] U. Teubner and P. Gibbon, High-order harmonics from laser-irradiated plasma surfaces, Rev. Mod. Phys. **81**, 445 (2009).

[7] V. A. Vshivkov, N. M. Naumova, F. Pegoraro, and S. V. Bulanov, Nonlinear electrodynamics of the interaction of ultra-intense laser pulses with a thin foil, Phys. Plasmas **5**, 2727 (1998).

[8] S. V. Bulanov, T. Zh. Esirkepov, M. Kando, S. S. Bulanov, S. G. Rykovanov, and F. Pegoraro, Strong field electrodynamics of a thin foil, Phys. Plasmas **20**, 123114 (2013).

[9] S. V. Bulanov, N. M. Naumova, and F. Pegoraro, Interaction of an ultrashort, relativistically strong laser pulse with an overdense plasma, Phys. Plasmas **1**, 745 (1994).

[10] B. Dromey, M. Zepf, A. Gopal, K. Lancaster, M. S. Wei, K. Krushelnick, M. Tatarakis, N. Vakakis, S. Moustaizis, R. Kodama, M. Tampo, C. Stoeckl, R. Clarke, H. Habara, D. Neely, S. Karsch, and P. Norreys, High harmonic generation in the relativistic limit, Nat. Phys. **2**, 456 (2006).

[11] S. V. Bulanov, T. Esirkepov, and T. Tajima, Light intensification towards the Schwinger Limit, Phys. Rev. Lett. **91**, 085001 (2003).

[12] L. Chopineau, A. Leblanc, G. Blaclard, A. Denoeud, M. Thévenet, J-L. Vay, G. Bonnaud, Ph. Martin, H. Vincenti, and F. Quéré, Identification of coupling mechanisms between ultraintense laser light and dense plasmas, Phys. Rev. X **9**, 011050 (2019).

[13] P. Gibbon, D. Altenbernd, U. Teubner, E. Förster, P. Audebert, J.-P. Geindre, J.-C. Gauthier, and A. Mysyrowicz, Plasma density determination by transmission of laser-generated surface harmonics, Phys. Rev. E **55**, R6352 (1997).

[14] R. Hässner, W. Theobald, S. Niedermeier, H. Schillinger, and R. Sauerbrey, High-order harmonics from solid targets as a probe for high-density plasmas, Opt. Lett. **22**, 1491 (1997).

[15] E. C. Jarque and L. Plaja, Harmonic filtering in an optically thin laser-generated plasma, Phys. Rev. E **58**, 7864 (1998).

[16] K. Krushelnick, W. Rozmus, U. Wagner, F. N. Beg, S. G. Bochkarev, E. L. Clark, A. E. Dangor, R. G. Evans, A. Gopal, H. Habara, S. P. D. Mangles, P. A. Norreys, A. P. L. Robinson, M. Tatarakis, M. S. Wei, and M. Zepf, Effect of Relativistic Plasma on Extreme-Ultraviolet Harmonic Emission from Intense Laser-Matter Interactions, Phys. Rev. Lett. **100**, 125005 (2008).

[17] F. Quéré, C. Thaury, P. Monot, S. Dobosz, Ph. Martin, J.-P. Geindre, and P. Audebert, Coherent Wake Emission of High-Order Harmonics from Overdense Plasmas, Phys. Rev. Lett. **96**, 125004 (2006).

[18] H. George, F. Quéré, C. Thaury, G. Bonnaud, and Ph. Martin, Mechanisms of forward laser harmonic emission from thin overdense plasmas, New J. Phys. **11**, 113028 (2009).

[19] D. an der Brügge and A. Pukhov, Enhanced relativistic harmonics by electron nanobunching, Phys. Plasmas **17**, 033110 (2010).

[20] B. Dromey, S. Rykovanov, M. Yeung, R. Hörlein, D. Jung, D. C. Gautier, T. Dzelzainis, D. Kiefer, S. Palaniyppan, R. Shah, J. Schreiber, H. Ruhl, J. C. Fernandez, C. L. S. Lewis, M. Zepf, and B. M. Hegelich, Coherent synchrotron emission from electron nanobunches formed in relativistic laser-plasma interactions, Nat. Phys. **8**, 804 (2012).

[21] Y. Jiang, Z.-Y. Chen, Z. Liu, L. Cao, C. Zheng, R. Xie, Y. Chao, and X. He, Direct generation of relativistic isolated attosecond pulses in transmission from laser-driven plasmas, Opt. Lett. **46**, 1285 (2021).

[22] Y. Shou, R. Hu, Z. Gong, J. Yu, J. erh Chen, G. Mourou, X. Yan, and W. Ma, Cascaded generation of isolated sub-10 attosecond half-cycle pulses, New J. Phys. **23**, 053003 (2021).

[23] M. Yeung, B. Dromey, S. Cousens, T. Dzelzainis, D. Kiefer, J. Schreiber, J. H. Bin, W. Ma, C. Kreuzer, J. Meyer-ter-Vehn, M. J. V. Streeter, P. S. Foster, S. Rykovanov, and M. Zepf, Dependence of Laser-Driven Coherent Synchrotron Emission Efficiency on Pulse Ellipticity and Implications for Polarization Gating, Phys. Rev. Lett. **112**, 123902 (2014).

[24] M. V. Arkhipov, R. M. Arkhipov, A. V. Pakhomov, I. V. Babushkin, A. Demircan, U. Morgner, and N. N. Rosanov, Generation of unipolar half-cycle pulses via unusual reflection of a single-cycle pulse from an optically thin metallic or dielectric layer, Opt. Lett. **42**, 2189 (2017).

[25] A. S. Moskalenko, Z.-G. Zhu, and J. Berakdar, Charge and spin dynamics driven by ultrashort extreme broadband pulses: A theory perspective, Phys. Rep. **672**, 1 (2017).

[26] I. Thiele, E. Siminos, and T. Fülöp, Electron Beam Driven Generation of Frequency-Tunable Isolated Relativistic Subcycle Pulses, Phys. Rev. Lett. **122**, 104803 (2019).

[27] T. D. Arber, K. Bennett, C. S. Brady, A. Lawrence-Douglas, M. G. Ramsay, N. J. Sircombe, P. Gillies, R. G. Evans, H. Schmitz, A. R. Bell, and C. P. Ridgers, Contemporary particle-in-cell approach to laser-plasma modelling, Plasma Phys. Control. Fusion **57**, 113001 (2015).

[28] Y. X. Zhang, S. Rykovanov, M. Shi, C. L. Zhong, X. T. He, B. Qiao, and M. Zepf, Giant Isolated Attosecond Pulses from Two-Color Laser-Plasma Interactions, Phys. Rev. Lett. **124**, 114802 (2020).

[29] M. Cherednychek and A. Pukhov, Analytical approach to high harmonics spectrum in the nanobunching regime, Phys. Plasmas **23**, 103301 (2016).

[30] S. Gordienko and A. Pukhov, Scalings for ultrarelativistic laser plasmas and quasimonoenergetic electrons, Phys. Plasmas **12**, 043109 (2005).

[31] T. Baeva, S. Gordienko, and A. Pukhov, Theory of high-order harmonic generation in relativistic laser interaction with overdense plasma, Phys. Rev. E **74**, 046404 (2006).

[32] X. Xu, B. Qiao, T. Yu, Y. Yin, H. Zhuo, K. Liu, D. Xie, D. Zou, and W. Wang, The effect of target thickness on the efficiency of high-order harmonics generated from laser-driven overdense plasma target, New J. Phys. **21**, 103013 (2019).